Single-Step Synthesis of SnS_2 Nanosheet-Decorated TiO_2 Anatase Nanofibers as Efficient Photocatalysts for the Degradation of Gas-Phase Diethylsulfide

Konstantinos C. Christoforidis, Armelle Sengele, Valérie Keller, and Nicolas Keller*

Institut de Chimie et Procédés pour l'Energie, l'Environnement et la Santé (ICPEES), CNRS, University of Strasbourg, 25 rue Becquerel, 67087 Strasbourg, France

Supporting Information

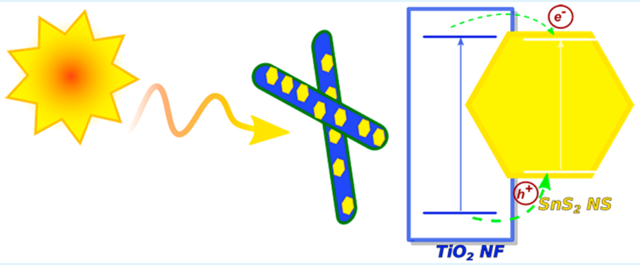

ABSTRACT: We report on a facile one-step soft hydrothermal process for synthesizing 1D anatase TiO_2 nanofibers decorated with ultrathin SnS_2 nanosheets. H-titanate nanofibers were used as preshaped Ti precursor. Under controlled conditions, the H-titanate structure was transformed into anatase maintaining the fibril morphology, while at the same time SnS_2 nanosheets were grown in situ on the surface of the nanofibers. The successful formation of SnS_2 nanosheets on the TiO_2 nanofibers was confirmed by high-resolution TEM, and together with XPS spectroscopy, the tight interface formed between the SnS_2 and the anatase TiO_2 nanofibers was verified. The 1D SnS_2/TiO_2 hierarchical nanostructures with semiconductor heterojunction were proven to be very efficient under artificial solar irradiation in the photocatalytic degradation of gaseous diethylsulfide as simulant for live yperite chemical warfare agent as well as model substrate for malodorous organosulfide volatile organic compounds. SnS_2 did not operate as a visible light sensitizer for TiO_2 but rather as an oxidizing agent and charge-carrier separator. The semiconductor ratio in the heterostructure controlled the photoactivity. Samples with no or high content of SnS_2 were less active than those with moderate SnS_2 content. Enhanced reactivity was ascribed to an efficient separation of the photogenerated charge carriers driven by the differences in band edge positions and favored by the tight interface within the coupled heterostructure.

KEYWORDS: *SnS_2, TiO_2, photocatalysis, heterojunction, H-titanate, hierarchical nanostructure, chemical warfare agents, diethylsulfide degradation*

INTRODUCTION

The threat and global concern of chemical warfare agents (CWA) has been largely increased over the last decades. The use of sorbents as decontaminating agents either as a real-time or a post-treatment method is certainly not considered an effective process. The use of catalytic systems capable of degrading instead of only storing CWA is definitely the method of choice for efficient and realistic applications.[1] Toward this scenario, photocatalysis using semiconductor materials and solar energy as the energy source has been established as an attractive method for environmental and human health protection.[2] Titanium dioxide (TiO_2) is the most frequently employed semiconductor photocatalyst because of its inherent physicochemical properties. It is an environmental friendly, nontoxic, and low-cost material with high stability under working conditions. These, together with the potential of complete mineralization of contaminants without yielding toxic byproducts make TiO_2 a perfect candidate for CWA degradation.[3−12]

Among the different polymorphs of TiO_2, the anatase structure is generally preferred in photocatalysis mostly because of its charge carrier handling properties compared to the other TiO_2 phases.[13,14] However, TiO_2 is a wide band-gap semiconductor (~3.2 eV for anatase) and exhibits a relatively fast recombination rate of electron−hole pairs. Given that photocatalytic efficiency of titania in organic degradation reactions is usually defined by the abundance and stability of the photogenerated charges (electron and holes), efforts have been devoted to extending the lifetime of such charge carriers. Many approaches have been investigated, including the modification of the shape of the nanoparticles for the development of 1D nanomaterials or of their chemical compositions through the design and fabrication of semiconductor heterostructures, hybrid nanocomposites, doped-TiO_2 nanostructures, or multiphase materials.[13,15−24] Numerous studies have been carried out on charge trapping and recombination[24−26] as well as on understanding the factors affecting such processes.[24,27,28]

On the basis of the drawbacks of pure TiO_2-based materials, semiconducting metal sulfides have the ability to absorb light in

Received: June 18, 2015
Accepted: August 11, 2015
Published: August 11, 2015

the visible region because of their relatively narrow band gap.[29−32] They are considered a promising class of materials and have been used as sunlight-activated photocatalysts and efficient separators of photogenerated charges in coupled heterostructures.[29,32−37] Among them, CdS has been mostly studied. However, CdS is far from any realistic application because of its high toxicity. By contrast, SnS_2 gained interest as being a nontoxic, inexpensive, and chemically stable IV−VI semiconductor, with a band gap within the range of 2.08−2.44 eV and a CdI_2-type layered structure.[31,32,37,38] Targeting environmental and energy-related reactions, processes have been recently implemented for the synthesis of SnS_2 of different morphologies as well as those coupled with semiconducting metal oxides and carbon-based materials (i.e., graphene and carbon nanotubes) for elaborating heterostructures and hybrid nanocomposites, respectively.[32,36−45] Via a two-step process, Zhang et. al synthesized SnS_2 nanosheets on the surface of preformed calcined electrospun anatase/rutile nanofibers, acting as light sensitizer and charge separator, and effectively applied in the degradation of dyes and phenols.[37]

Toward the main challenges of expanding the photoresponse of catalysts for solar light use and of reducing their charge recombination rates, different approaches have been adopted, frequently involving multistep synthesis routes, high-temperature treatments, or the use of sacrificial chemical additives as structural promoter or noble metal nanoparticles as charge recombination inhibitors.[19,20] Herein, we report a facile and cost-effective one-step soft hydrothermal method for the synthesis of 1D SnS_2/anatase TiO_2 hierarchical nanostructures starting from a preshaped H-titanate precursor without the need of any calcination step, stabilization agents, or surfactants. The prepared photocatalysts were proven to be highly efficient under artificial solar light irradiation against the gas-phase degradation of diethylsulfide (DES), acting as a simulant for the live yperite CWA, a blister agent also known as mustard gas. DES is also a suitable model substrate for malodorous organosulfide volatile organic compounds. Photocatalysis has already been successfully used for degrading organosulfur compounds such as DES and also scarcely directly applied on live blister yperite CWA.[4−10] One should note the interesting studies carried out on the photocatalytic oxidation of nauseous organosulfides such as dimethylsulfides.[46]

EXPERIMENTAL SECTION

Material Synthesis. *Preparation of the Ti Precursor.* All chemicals were used as received without further purification. For the synthesis of H-titanate, 5 g of commercial Aeroxide TiO_2 P-25 (Evonik) powder was hydrothermally treated at 180 °C for 48 h in 70 mL of 10 M NaOH aqueous solution. The mixture was first sonicated for 30 min and stirred magnetically for 1 h before being transferred into a 120 mL Teflon-lined stainless-steel autoclave. After synthesis, the autoclave was naturally cooled to room temperature, and the obtained solid was rinsed with 1 M HCl. This process exchanges Na^+ with H^+. Then, the solid was washed with distilled water until the pH of the washing solution was neutral, and the resulting powder was dried at 100 °C. This material was used as preshaped Ti precursor for the synthesis of the 1D coupled SnS_2/TiO_2 photocatalysts.

Synthesis of the SnS_2/TiO_2 and SnS_2 Nanostructures. A 0.4 g portion of the as-synthesized H-titanate material was hydrothermally treated in a Teflon-lined stainless-steel autoclave at 160 °C for 12 h in an aqueous solution of $SnCl_4$ (Sigma-Aldrich, 99%) and thioacetamide (TAA, Aldrich, 99%). The $SnCl_4$/TAA molar ratio was kept constant at 0.1 in all samples, whereas the concentration of $SnCl_4$ varied to achieve a nominal Sn/Ti molar ratio of 0.14, 0.20, and 0.38 (samples named SnTi-A, SnTi-B, and SnTi-C, respectively) considering $H_2Ti_3O_7$ as the structure of the Ti precursor. After naturally cooling the autoclave to room temperature, the solid was collected, washed several times with distilled water, and finally dried at 80 °C. In a similar way, pure SnS_2 nanosheets were synthesized in the absence of H-titanate. As reference, the as-synthesized H-titanate material was also calcined at 380 °C for 2 h in air using a ramp of 2 °C/min. A moderate calcination temperature was chosen ensuring the transition of the parent H-titanate structure to TiO_2 without causing the breaking of the nanofiber structure, thus maintaining its 1D morphology. Under these conditions, the calcination step led to the formation of TiO_2 B-form. (See XRD and Raman data.)

Instrumentation. UV−vis absorption spectra of the materials were recorded on a Varian Cary 100 Scan spectrophotometer equipped with a DRA-CA-301 Labsphere diffuse reflectance cell. BET surface area measurements were carried out by N_2 adsorption at 77 K using a ASAP2010 Micromeritics Tristar apparatus. Powder X-ray diffraction (XRD) measurements were carried out on a D8 Advance Bruker diffractometer with a Cu Kα X-ray source. Raman spectra were collected with a LabRaman ARAMIS instrument using a 532 nm laser. Care was given during use of the working laser power to avoid any heating effect. Bulk atomic ratios were derived from inductively coupled plasma atomic emission spectroscopy analysis. X-ray photoelectron spectroscopy (XPS) characterization was carried out on a Multilab 2000 (Thermo) spectrometer equipped with Al Kα anode ($h\nu$ = 1486.6 eV). The energy shift due to electrostatic charging was subtracted using the contamination carbon C 1s band at 284.6 eV. Surface atomic ratios were derived from XPS spectra considering an S-shaped Shirley-type background using the appropriate experimental sensitivity factors as determined by Scofield.[47]

Scanning electron microscopy (SEM) was carried out in secondary electron mode on a JEOL-JSM-6700 F FEG microscope. Prior to analysis, the samples were coated with gold. Transmission electron microscopy (TEM) was carried out on a Topcon 002B microscope operating at 200 kV with a point-to-point resolution of 0.18 nm. The sample was sonicated in ethanol before a drop of the solution was deposited onto a holey carbon film on a copper grid for observation.

Photocatalytic Activity Evaluation. Gas-phase photocatalytic activity tests were carried out in a 265 mm length single-pass annular Pyrex reactor made of two coaxial tubes 3 mm apart (i.d. 22 mm and e.d. 28 mm), between which the reactant mixture was passing through. Extensive details concerning both photocatalytic reactor and device can be found elsewhere.[48] A 100 mg amount of the photocatalysts, corresponding to a surface density of 0.23 mg/cm^2, was evenly coated as a thin film on the internal side of the external tube by evaporating a catalyst-containing aqueous suspension to dryness. The reactor coated with the catalyst was finally dried at 110 °C for 1 h in air. DES (Aldrich, 98%) and water were fed at ambient temperature and atmospheric pressure by bubbling air through two saturators and mixed with additional air to obtain the required DES−water−air ratios with a constant total air flow. Standard conditions were: 675 ppm$_v$ DES inlet concentration, 40% relative humidity, and 100 cm^3/min total flow. After exposing the catalyst to the mixture until dark-adsorption equilibrium was reached (control test), the catalyst was irradiated by a commercial 24 W solar-light-simulating lamp (Philips DeLuxe pro LTJHo, Figure S1) located inside the inner tube of the reactor so that the external surface of the thin film was exposed to an irradiance of 3.3 mW/cm^2. The catalytic activity was evaluated under steady-state conditions, typically achieved after a few hours of irradiation. No changes in activity were detected for all samples within 24 h after reaching steady-state conditions, suggesting that the catalysts prepared are stable under the conditions of our experiment. Reactants and reaction products were analyzed online by an Agilent GC-6890 N Gas Chromatograph equipped with HP Plot Q and HP-5MS columns, coupled to a thermal conductivity detector and a MS-5973N Mass Spectrometer, respectively.

RESULTS AND DISCUSSION

The phase composition and the crystal structure of the nanomaterials were studied by XRD. Figure 1 presents the

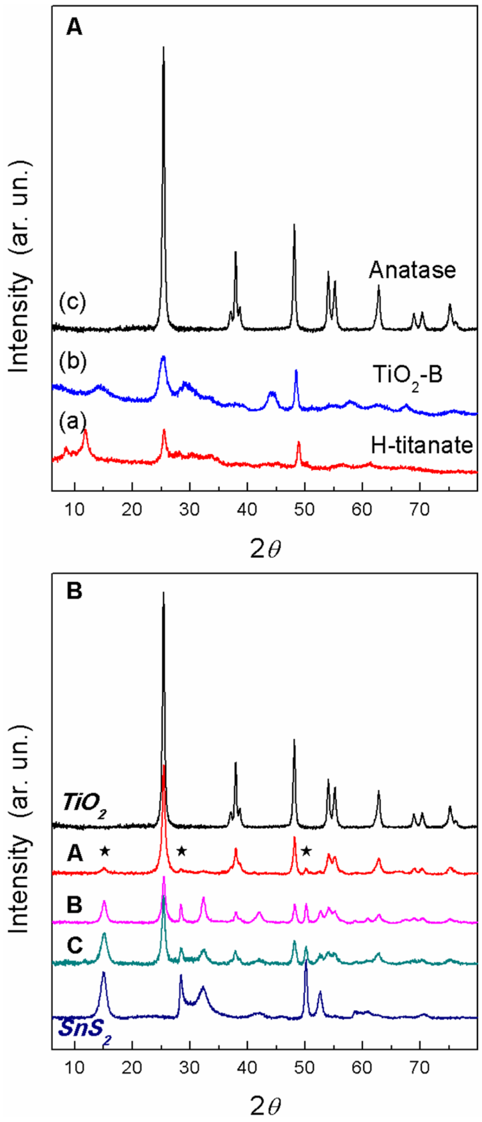

Figure 1. (A) XRD patterns of (a) pristine Ti-nanofibers (H-titanate structure), (b) H-titanate after calcination at 380 °C (TiO_2 B-form), and (c) H-titanate after hydrothermal treatment in the absence of Sn^{4+} and thioacetamide (anatase TiO_2). (B) XRD patterns of the pure TiO_2 and SnS_2 and the SnS_2/TiO_2 nanostructures after hydrothermal treatment. Spectra A−C correspond to the SnTi-A, SnTi-B, and SnTi-C samples, respectively. Symbols indicate the peaks of SnS_2 in the SnTi-A sample.

XRD patterns of pure Ti materials (Figure 1A) and of Sn−Ti catalysts (Figure 1B). On the basis of XRD pattern, the hydrothermal treatment of Aeroxide TiO_2 P-25 resulted in the formation of a layered H-titanate (Figure 1A, pattern a) with a monoclinic lattice ($C2/m$).[49,50] This material was used as the Ti precursor for synthesizing the other photocatalysts. Calcination of the pristine H-titanate nanomaterial at 380 °C led to the formation of TiO_2 B-form (Figure 1A, pattern b).[50] In contrast, hydrothermal treatment of the pristine H-titanate material in the absence of any Sn^{4+} and thioacetamide (TAA) resulted in the formation of pure anatase (Powder Diffraction File (PDF-2) no. 21-1272, International Centre for Diffraction Data (ICCD), [2004]). In Figure 1B, the XRD pattern of the Sn−Ti nanostructures obtained after hydrothermal treatment of the pristine H-titanate nanomaterial in the presence of Sn^{4+} and TAA could be fully indexed to pure anatase TiO_2 and hexagonal SnS_2 (Berndtite-2T, PDF-2 no. 83-1705, ICCD, [2004]). SnS_2 possess a 2D CdI_2 layered structure in which the individual layers are held together via van der Waals interactions. No peaks attributed to tin oxide were observed, and in the final SnS_2/TiO_2 nanostructures, the position of the diffraction peaks of pure SnS_2 and anatase TiO_2 were retained.

The phase composition of the prepared nanomaterials was further studied through the more sensitive Raman spectroscopy. Figure 2A provides an additional evidence for the H-trititanate structure of the Ti precursor, the TiO_2 anatase phase after the Sn- and TAA-free hydrothermal treatment of the as-

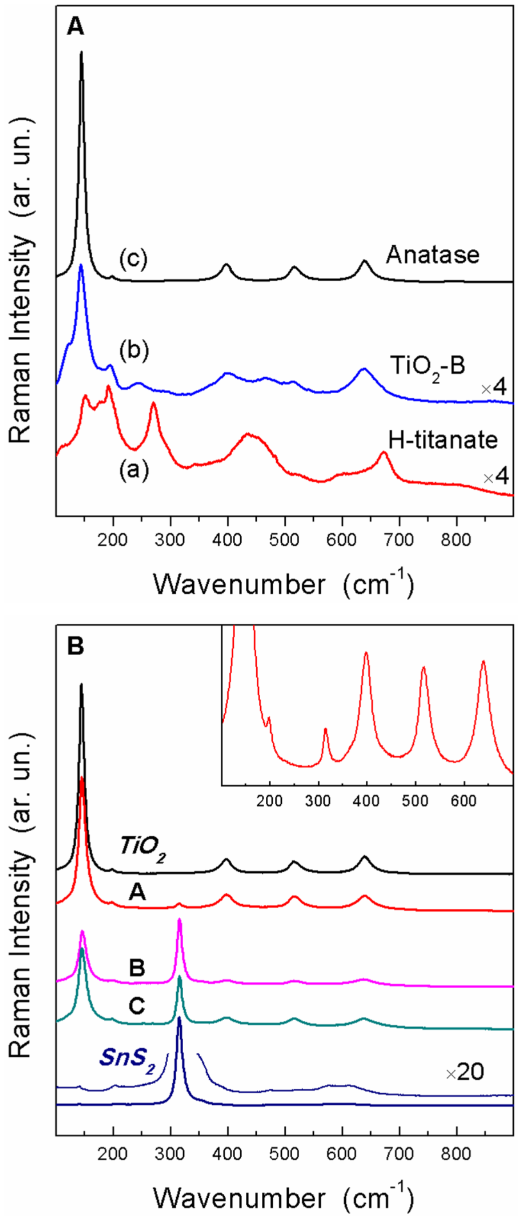

Figure 2. (A) Raman spectra of (a) pristine Ti-nanofibers (H-titanate structure), (b) H-titanate after calcination at 380 °C (TiO_2 B-form), and (c) H-titanate after hydrothermal treatment in the absence of Sn^{4+} and thioacetamide (anatase TiO_2). (B) Raman spectra of the pure TiO_2 and SnS_2 and the SnS_2/TiO_2 nanostructures after hydrothermal treatment. Spectra A−C correspond to the SnTi-A, SnTi-B, and SnTi-C samples, respectively. A high-resolution view of the pure SnS_2 spectrum is also provided. The inset displays a closer view of the SnTi-A spectrum.

synthesized H-trititanate Ti precursor, and the TiO_2 B-form after its direct calcination.[50] Raman spectra of the pure TiO_2 and SnS_2 and the SnS_2/TiO_2 materials after hydrothermal treatment further confirmed the exclusive presence of TiO_2 anatase phase and SnS_2 (Figure 2B). The peaks centered at ca. 144, 195, 399, 517, and 639 cm^{-1}, correspond to the $E_g(1)$, $E_g(2)$, $B_{1g}(1)$, $B_{1g}(2)$, $A_{1g}(1)$ and $E_g(3)$ modes of anatase, respectively.[51] The high-intensity peak centered at 314 cm^{-1} and the low-intensity peak around 210 cm^{-1} correspond to the first-order A_{1g} and E_g modes of hexagonal SnS_2 phase, respectively, according to the group theory analysis. In addition, a weak peak at 137 cm^{-1} and broad peaks in the range 470−630 cm^{-1} were detected and ascribed to second-order effects. (See the SnS_2 high-resolution spectrum in Figure 2B.)[43,52,53] No peaks attributed to SnO_2 were observed, nor were any broad Raman band that could be ascribed to amorphous tin(IV)-hydrous oxide. Both Raman and XRD characterizations indicated the purity of the SnS_2/TiO_2 nanostructures synthesized under the hydrothermal condition applied.

Calcining the pristine H-titanate nanomaterial at 380 °C leads to the formation of TiO_2 B-form instead of anatase on the basis of XRD and Raman data (Figures 1A and 2A).[50] The TiO_2 B-form is generally much less active compared to anatase (seen in the following).[54] This is a first important observation because on the contrary the desired TiO_2 anatase phase is obtained after the hydrothermal treatment of the pristine H-titanate.

The morphology of the prepared materials was studied by SEM and the more accurate TEM. Representative SEM images shown in Figure 3 evidenced the 1D morphology of the nanomaterials prepared starting from H-titanate materials. Figure 3a shows the fibril morphology of the raw H-titanate material, with the complete transformation of the Aeroxide TiO_2 P-25 nanoparticles into long fibers under the hydrothermal conditions applied. The fibril morphology of the pristine H-titanate was maintained during the calcination step, leading to the formation of TiO_2 B-form (Figure 3b), as well as during the hydrothermal treatment in the presence of Sn^{4+} and TAA (Figure 3c,d). However, the surface of the materials within the SnS_2/TiO_2 series became rougher compared to that of both the pure H-titanate Ti precursor and the calcined TiO_2 B-form reference material.

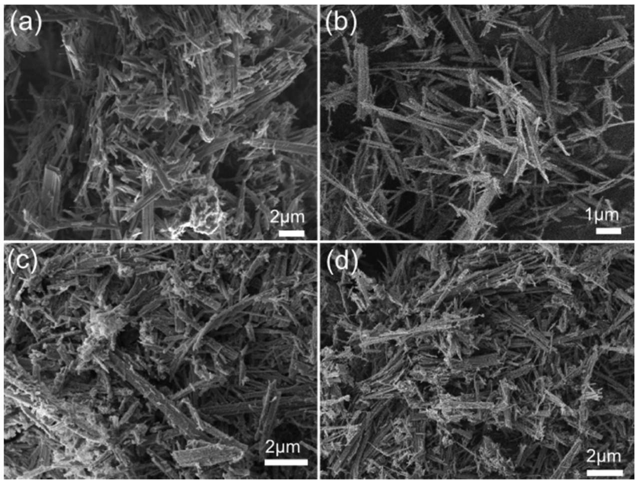

Figure 3. SEM images of (a) pristine H-titanate nanofibers, (b) H-titanate nanofibers calcined at 380 °C (TiO_2 B-form), and (c and d) SnS_2/anatase nanofibers obtained after hydrothermal treatment in the presence of Sn^{4+} and thioacetamide (SnTi-A and SnTi-B samples, respectively).

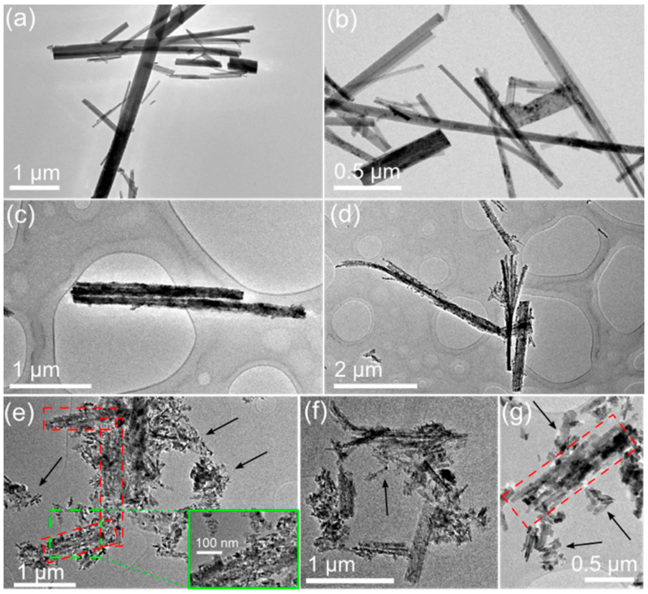

Figure 4. Low-magnification TEM images of (a) pristine H-titanate nanofibers, (b) SnTi-A, (c) SnTi-B, and (d) SnTi-C after hydrothermal treatment; (e−g) pure anatase TiO_2 after hydrothermal treatment. Inset in (e): high-magnification image of the area marked with green rectangle, indicating within the pure anatase TiO_2 sample the simultaneous presence of nanofibers (red rectangles), broken nanofibers, and monodispersed TiO_2 nanocrystals (indicated by arrows).

Figure 4 presents low-magnification TEM images of the parent H-titanate nanofibers (Figure 4a), the SnS_2/TiO_2 nanostructures (Figure 4b−d), and the pure anatase TiO_2 (Figure 4e−g) obtained under hydrothermal treatment. The distinct fibrous morphology can be observed. The pristine H-titanate Ti precursor had a smooth surface and rigid crystal structure, with a fiber aspect ratio over 90 resulting from fiber lengths ranging from hundreds of nanometers to several micrometers and an average diameter of 75 nm (fiber diameters within the 40−300 nm range). Their BET specific surface area of 37 m^2/g further confirmed the high crystallinity of the prepared titanate fibers. After hydrothermal treatment in the presence of Sn and TAA, the TEM images confirmed that the SnS_2/TiO_2 nanostructures retained the fibril morphology of the parent titanate material, however with a rougher exposed surface (Figure 4b−d). Beside the large majority of fibril SnS_2/TiO_2 nanostructures, smaller nanofibers could also be observed, in a more pronounced way when the SnS_2 content was low (SnTi-A vs SnTi-B and -C). This is most likely due to the breaking of thin and less-crystallized titanate fibers during the hydrothermal treatment as was previously observed in similar H-titanate fibers subjected to analogous treatment.[55] In the pure TiO_2 sample, monodispersed nanocrystals were also observed (Figure 4e−g, indicated by the arrows). Although it is outside the scope of the present work, with the data in hand we cannot conclude any final answer, though we suspect that the breaking of the nanofiber morphology of the parent H-titanate into small nanofibers or even into monodispersed nanocrystals (in the case of pure anatase TiO_2 nanomaterial) is related to the low amount or even the absence of the organic part (TAA) during the synthesis.

The high-magnification TEM images of the pure SnS_2 sample shown in Figure 5 evidence the characteristic formation of hexagonal SnS_2 nanosheets (NS), with an average lateral size of 22 ± 5 nm and an average thickness of 7.2 ± 2 nm. The high-resolution TEM (HRTEM) image of the SnS_2 nanosheet top view (area labeled A) with an interplanar distance of 0.315 nm is consistent with the (100) plane of hexagonal SnS_2, whereas the 0.59 nm fringe interval of the SnS_2 nanosheet side view (area labeled B) coincides with the *d*-spacing of the (001) plane.[37,39] The corresponding fast Fourier transform (FFT) pattern of the top view is characteristic of the (100) plane in hexagonal SnS_2. These data suggest that SnS_2 nanosheets possess a 2D layered structure, forming nanosheets with restricted growth along the [001] direction.

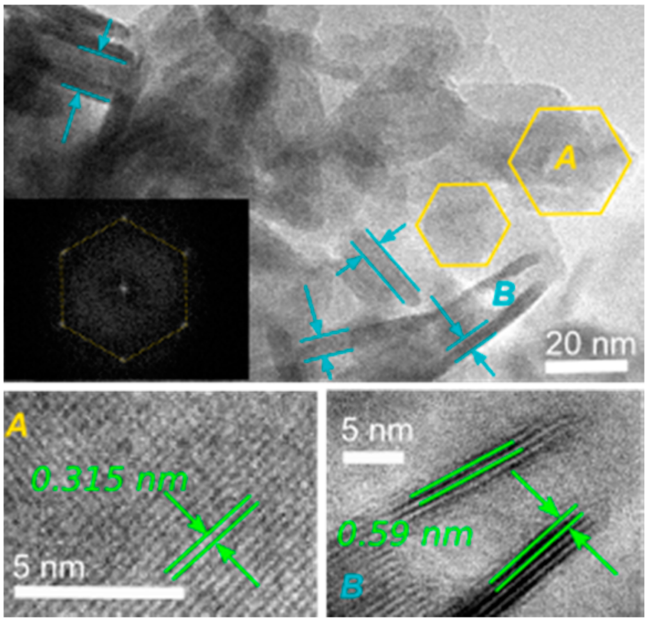

Figure 5. (top) TEM images of the pure SnS_2 nanosheets (NS) together with a fast Fourier transform (FFT) pattern of the top view of an individual SnS_2 NS. (bottom) HRTEM images of the marked areas, with (A) top and (B) side views of SnS_2 NS.

Figure 6 presents high-magnification TEM images of the SnS_2/TiO_2 nanostructures. The presence of SnS_2 nanosheets on the surface of the TiO_2 nanofibers is evidenced (Figure 6a,b). This observation confirms the formation of a hierarchical structure under the hydrothermal conditions applied, where the SnS_2 nanosheets are placed on the surface of the TiO_2 nanofibers. Within the core of the nanofibers, the fringes parallel to the nanofiber axis in the insets in Figure 6a correspond to an interplanar distance of 0.35 nm, characteristic of the (101) plane in the anatase crystal phase. It was observed continuously throughout the nanofiber, indicating the possible formation of a singly crystalline structure with preferred growth along the [001] direction (Figure 6a, insets).[56,57]

The heterojunction region in the SnS_2/TiO_2 nanostructures is also displayed in the high-magnification TEM images in Figure 6. In the HRTEM image (left inset), the 0.59 nm fringe interval of the SnS_2 (001) plane and the 0.35 nm fringe interval of the (101) plane of anatase TiO_2 suggested that the flat-lying SnS_2 nanosheets were interfaced through the (001) plane of SnS_2 with the TiO_2 nanofibers exposing the (101) plane of TiO_2 anatase. The EDX spectrum (Figure 6c) revealed that the SnS_2/TiO_2 nanostructures are composed solely of Ti, O, Sn, and S. No Na was detected, verifying the successful exchange with H^+ during the acidic washing of the titanate fibers. These observations confirmed the successful decoration of the nanofibers with SnS_2 nanosheets and suggest a strong interfacial interaction (i.e., a tight interface) that is expected to have an impact on the photoactivity of the prepared hierarchical structures.

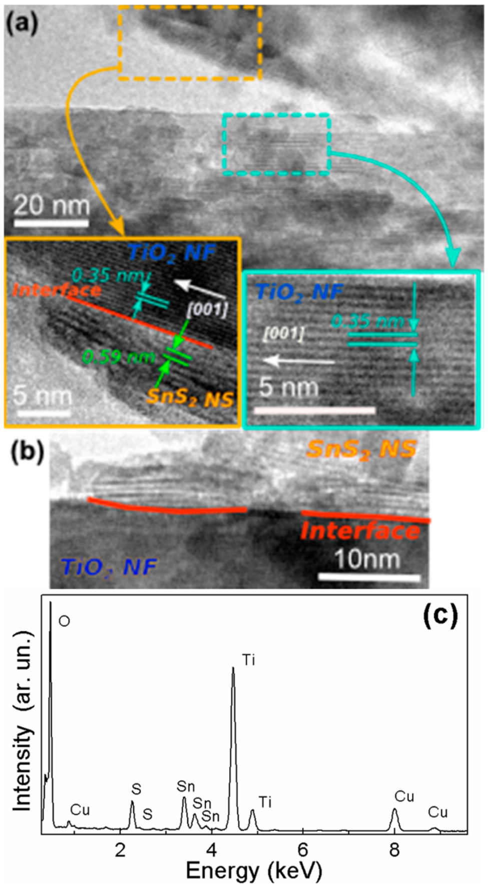

Figure 6. High-magnification TEM images of (a) SnTi-B and (b) SnTi-C nanomaterials. The insets are HRTEM images of the SnTi-B sample corresponding to the areas marked with the rectangles. (c) Associated EDX spectrum recorded on an individual nanofiber of the SnTi-B sample. The Cu peaks in the EDX spectrum originate from the TEM grid.

It should be noted that anatase TiO_2 and H-titanate structure have the TiO_6 octahedra as common basic structural units. On the basis of the morphological characteristics of the prepared materials, the transition from titanate to anatase has been proposed to take place through two different mechanisms depending on the size and crystallinity of the parent titanate material. In the in situ topochemical transformation mechanism,[58] the pristine morphology of the Ti precursor is maintained. The second mechanism involves the dissolution of the titanate precursor and the formation of anatase through recrystallization, resulting in distinct morphologies compared with that of Ti precursor.[49,59] Given that the 1D morphological characteristics of the parent H-titanate material were maintained in the SnS_2/TiO_2 nanostructures, we propose that the phase transition from H-titanate to pure anatase is due to a topochemical reaction. This would also guarantee the absence of any impurity within the bulk of TiO_2 nanofibers after the second hydrothermal treatment in the presence of Sn^{4+} and TAA because only surface modification of preshaped nanofibers could occur.

The surface composition and chemical state were further investigated by means of XPS. In the XPS survey spectra, no obvious impurity could be detected. In the pure TiO_2 sample, the single contribution with a peak doublet at 458.5 and 464.2 eV (Table S1) and a spin−orbit splitting of 5.7 eV was ascribed to the Ti $2p^{3/2}$−Ti $2p^{1/2}$ spin−orbit components of Ti^{4+} (Ti−O) surface species in TiO_2 (Figure 7a). The O 1s peaks (Figure 7c) of the different TiO_2-containing nanostructures were fitted using three contributions at 529.7, 531.3, and 533.0 eV, attributed to the lattice oxygen ions of the anatase network, surface hydroxyl groups, and adsorbed water molecules, respectively.[60] In the pure SnS_2 sample, the Sn $3d^{5/2}$ and $3d^{3/2}$ doublet centered at 486.4 and 494.8 eV (spin−orbit coupling of 8.4 eV) corresponds to Sn^{4+} (Figure 7b), and the peaks located at 161.3 and 162.4 eV were ascribed to the S $2p^{3/2}$ and $2p^{1/2}$ orbitals, with a spin−orbit splitting of 1.1 eV (Figure 7d). These binding energies are in agreement with the values reported for pure TiO_2 and SnS_2[39,61] and evidence the exclusive presence of Ti^{4+}, Sn^{4+}, and S^{2-}.

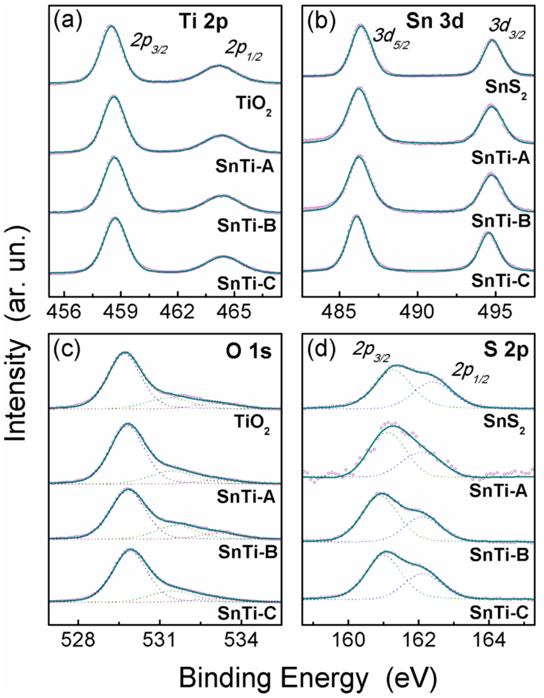

Figure 7. XPS spectra of the prepared nanostructures, i.e., pure TiO_2 and SnS_2 and SnTi-A, SnTi-B, and SnTi-C SnS_2/TiO_2 in (a) Ti 2p, (b) Sn 3d, (c) O 1s, and (d) S 2p regions. Symbols: experimental data; lines: fitting.

In the SnS_2/TiO_2 nanostructures, like for pure TiO_2 and SnS_2, a single doublet with adequate full width at half-maximum and spin−orbit coupling was used to fit Ti 2p (as Ti^{4+} surface species in TiO_2), Sn 3d, and S 2p peaks (as Sn^{4+} and S^{2-} in SnS_2, respectively). In accordance with XRD and Raman results, this confirmed the absence of sulfate and the exclusive presence of Sn within the SnS_2 nanosheets, rather than as tin oxide or as substitutional cationic dopant in the TiO_2 phase, for which an additional Sn^{4+}−O^{2-} doublet would be observed. No contributions originating from mixed phases were observed, and the materials were composed from the two juxtaposed semiconductors forming SnS_2/TiO_2 heterojunctions. However, no SnS_2/TiO_2 interfacial bindings such as Ti−S, Ti−O−S, or Ti−O−Sn could be resolved within the resolution limits of the XPS analysis. Nevertheless, distinct differences in the binding energies are detected in the SnS_2/TiO_2 hierarchical nanostructures when compared with the respective pure nanostructures. In the SnS_2/TiO_2 hierarchical nanomaterials, a shift toward higher energies was observed for both the Ti 2p (0.2 ± 0.1 eV) and O 1s (0.2 ± 0.1 eV) peaks (Table S1). This was accompanied by a shift toward lower binding energies for both the Sn 3d and S 2p contributions (0.3 ± 0.1 eV). These changes can be assigned to the formation of an interface with strong interaction between the two semiconductors and can be rationalized in terms of differences in the Fermi energy levels of the two semiconductors, taking into account their tight interface. The opposite shifts observed in the SnS_2/TiO_2 nanostructures, i.e., increase of the Ti 2p and decrease of the Sn 3d and S 2p binding energies, was explained by the appearance of the electron-depleted and -enriched space charge zones at the TiO_2 and SnS_2 interfaces, respectively, resulting from the formation of the n−n heterojunction between TiO_2 and SnS_2 with lower Fermi level.[37,62] This behavior clearly suggests strong interfacial interaction between the two semiconductors, most likely caused through the successful formation of a heterojunction and is consistent with the HRTEM results. This suggests the presence of an effective path for charge carrier migration between the two semiconductors. However, this interfacial interaction between both semiconductor phases might not be directly evidenced by XPS because of the sensitivity limits of the technique as well as the interfacial location of atoms involved.

The chemical composition of the SnS_2/TiO_2 nanostructures was investigated by means of ICP-AES spectroscopy. The smaller bulk Sn/Ti atomic ratios compared to the nominal ones (Table S2) indicated that part of the initial added Sn^{4+} is lost during the synthesis and the washing process. This loss increased with increasing the initial Sn^{4+} concentration. It is worth nothing that the Sn/Ti surface atomic ratios of the SnS_2/TiO_2 nanostructures as estimated from the XPS spectra using the appropriate experimental sensitivity factors[47] are significantly higher than the bulk ones (Table S2). This difference may be attributed to the exclusive presence of SnS_2 on the surface of the TiO_2 nanofibers. For all SnS_2/TiO_2 heterostructures and the pure SnS_2 nanosheets, the S/Sn ratio was close to 2 (1.71−1.95).

In organic degradation reaction, the photocatalytic activity of a semiconductor is usually defined by its electronic properties linked with light absorption abilities and the efficient separation of the photogenerated electrons (e^-) and holes (h^+). The optical absorption of the prepared nanomaterials was evaluated by diffuse reflectance (DR)-UV−vis spectroscopy. The DR-UV−vis spectra of H-trititanate, TiO_2 B-form, and the pure anatase TiO_2 material exhibited an absorption band only in the UV region (Figure S2A). In contrast, the pure SnS_2 and SnS_2/TiO_2 nanostructures displayed clear light absorption abilities in the visible region (Figure S3A). This is evidenced even from the low SnS_2-loaded nanomaterial (SnTi-A). These results clearly demonstrate that in the SnS_2/TiO_2 hierarchical nanostructures the light absorption in the visible region can be exclusively attributed in the presence of the SnS_2 nanosheets. An interesting observation is that the spectra of the SnS_2/TiO_2

hierarchical nanostructures could not be reproduced from a simple linear combination of the pure SnS_2 and TiO_2 spectra. This may indicate the formation of a heterostructure with interfacial interaction as proposed by the HRTEM and XPS data.

The band gap energies (E_g) of the pure TiO_2 nanofibers and SnS_2 nanosheets can be estimated from their optical absorption edges using the following formula:

$$\alpha h\nu = B(\mathrm{hv} - E_g)^{n/2}$$

where $h\nu$, α and B represent the excitation energy, absorption coefficient, and a constant, respectively. SnS_2 and TiO_2 were considered direct (i.e., $n = 1$) and indirect (i.e., $n = 4$) semiconductors, respectively. Instead of α, the Kubelka–Munk function was applied[63−66]

$$F(R) = \frac{(1 - R)^2}{2R}$$

where R is the reflectance in order to eliminate any tailing contribution from the DR-UV–vis spectra. (See Supporting Information for details.) The E_g values estimated from the plot of $F(R)h\nu$ versus energy by extrapolating the linear part (Figures S2B and S3B). The E_g values extracted were 3.18 and 2.4 eV for the anatase TiO_2 and SnS_2 NS, respectively, falling within the values reported in the literature.[13,37,51,61] Compared to anatase (E_g = 3.18 eV), the band gap energy of the H-titanate Ti precursor and the B-form TiO_2 obtained after calcination was somehow moderated (3.26 and 3.06 eV, respectively).

Photocatalytic Activity. Figure 8A shows the gas-phase photocatalytic degradation of DES obtained under artificial solar light irradiation of the prepared materials and the commercial Aeroxide TiO_2 P-25 reference after steady-state conditions were reached, expressed versus the Sn/Ti surface atomic ratio derived from the XPS spectra. Representative DES degradation data as a function of time on-stream are illustrated in Figure S4 for selected materials, i.e., the most active SnTi-A photocatalyst, the TiO_2 P-25 reference, the SnS_2, and the H-titanate nanofibers; these evidenced the progressive time on-stream deactivation of the photocatalysts to achieve the steady-state level. A first important observation is that all hydrothermally treated Sn–Ti photocatalysts presented the same or higher activity compared with that of the standard TiO_2 P-25 reference. The photocatalytic activity of the SnS_2/TiO_2 hierarchical nanostructures gains more significance when compared with the pristine H-titanate sample, presenting up to eight times higher photocatalytic activity against DES degradation. In addition, all SnS_2/TiO_2 nanostructures showed higher activity than that of the pure SnS_2 sample, whereas the low-loaded SnTi-A sample was two times more active than Aeroxide TiO_2 P-25. Within the SnS_2/TiO_2 nanostructures, a clear tendency toward enhanced photocatalytic activity was observed with decreasing the SnS_2 content in the heterostructure. Because no important differences were detected in terms of BET specific surface area (Table S2), the differences in the activity of the SnS_2/TiO_2 photocatalysts are certainly not related with surface adsorption properties. In addition, the TiO_2 B-form, prepared by direct calcination of the pristine H-titanate material, presented low photocatalytic activity compared with that of the hydrothermally treated nanostructures.

The different active photocatalysts displayed a similar behavior in terms of time-evolution of the gaseous degradation products, and representative data in the case of the most active SnTi-A photocatalyst is shown in Figure 8B. DES degradation initially corresponded to the formation of CO_2 and alcetaldehyde, and the further decrease in CO_2 concentration with time on-stream was accompanied by the observation of a maximum in the concentration of acetaldehyde, the main reaction intermediate byproduct corresponding to DES partial oxidation. Total removal of sulfur was observed at the beginning of the test, before a maximum in the concentration of diethyldisulfide (the main carbon- and sulfur-containing reaction intermediate) and the formation of small amounts of SO_2 were observed in parallel to the decrease in both the DES removal efficiency and the mineralization rate.

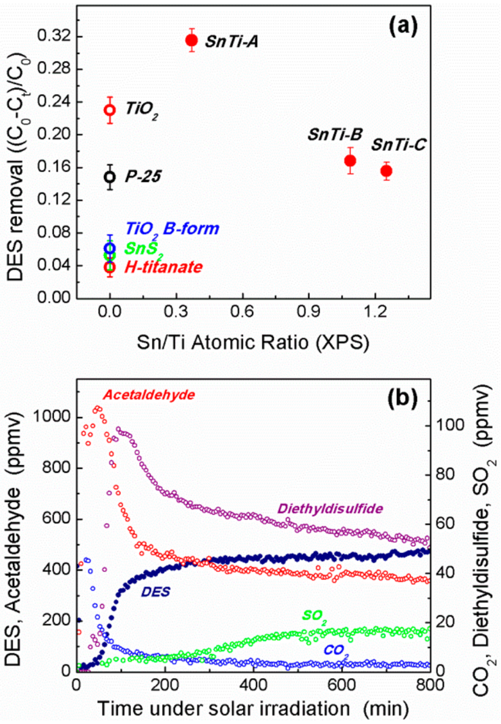

Figure 8. (a) Photocatalytic degradation of DES under artificial solar irradiation after steady-state conditions in DES conversion were achieved. Solid symbols: SnTi samples; open symbols: pure materials. Each symbol is labeled with the corresponding sample name. (b) Time on-stream evolution of DES reactant and of the gaseous reaction products formed during DES removal under artificial solar irradiation in the case of the SnTi-A photocatalyst. Reaction conditions: [DES] = 675 $\mathrm{ppm_v}$, 40% relative humidity, 100 cm^3/min total flow, solar light irradiance of 3.3 mW/cm^2.

Grandcolas et al. previously proposed a reaction mechanism,[5] considering as a first step either the direct oxidation of DES by photogenerated holes leading to diethylsulfinium radicals or its oxidation through hydroxyl radicals. Diethyldisulfide was proposed to result from the dimerization of the ethanethyl radical issued from C–S cleavage in the diethylsulfide radical cation. Hydroxyl radicals were proposed to oxidize the carbon in β position with formation of 3-(ethylthio)propanal or directly the sulfur atom with formation of diethylsulfoxide that undergoes further oxidation into diethylsulfone in the adsorbed phase, leading to ultimate oxidation into surface sulfate species.

The carbon balance was almost closed with the formation of acetaldehyde and CO_2, whereas the sulfur balance was only half-closed in gas phase with the formation of diethyldisulfide and SO_2. The formation at the photocatalyst surface of sulfate species as the ultimate sulfur-containing mineralization product of DES oxidation as well as the possible adsorption at the photocatalyst surface of sulfur-containing partially oxidized reaction intermediates was proposed for closing the sulfur balance.

The surface composition and chemical state of the photocatalysts after tests were evaluated by XPS. The Ti 2p and Sn 3d XPS spectra remained unchanged compared to those recorded on the fresh photocatalysts (Figure S5), verifying the stability of the nanomaterials under working conditions. By contrast, the S 2p XPS spectra of the used photocatalyst exhibited two contributions (Figure S6a, areas marked with rectangles). The first was identical with that of the fresh catalysts, corresponding to the S 2p doublet of the SnS_2 nanosheets. The second, located at higher energies, was related to the S $2p^{3/2}$−S $2p^{1/2}$ spin−orbit components assigned to surface S^{6+} sulfate species (Figure S6b).[5,67,68] Sulfate species accumulated on the surface of the catalyst and blocking the active sites of the photocatalyst have been reported to be responsible for the deactivation of the photocatalyst during the degradation of sulfur containing organic molecules and H_2S.[5,8,46,67,68] Furthermore, in the O 1s XPS spectra of the used catalysts, an additional contribution was detected at approximately 531.8 eV (Figure S6c) and assigned to surface O−S species. This additional contribution most likely originated from surface sulfates. One could also mention that the competition at the photocatalyst surface sites between both adsorption and reactivity of DES, and those of sulfur-containing partially oxidized reaction intermediates could contribute to the gradual activity decline observed with time on-stream from total degradation to stabilization.[5] Figure S7 presents the correlation plot between the photocatalytic activity in terms of DES removal efficiency at the steady-state and the relative content of the additional O 1s peak assigned to sulfate species observed in the used catalysts. The relative content of the extra peak (calculated as the percent of the total O 1s peak area without considering the H_2O contribution) is inversely proportional to the catalytic activity, suggesting the possible active site of the SnS_2/TiO_2 hierarchical nanostructure (i.e., on TiO_2 surface) and a possible deactivation mechanism through the adsorption of sulfates on the active sites.

The photocatalytic results in Figure 8 indicate a complicated process that can be explained considering the band edge position of the two semiconductors and the SnS_2 loading in the final architectures. The conduction and valence band (CB and VB, respectively) of SnS_2 and TiO_2 were estimated by the empirical equation[69]

$$E_{VB} = X - E_C + 0.5E_g$$

where E_{VB} is the VB edge potential, X is the electronegativity of the semiconductor, E_c is the energy of free electrons (4.5 eV on the hydrogen scale), and E_g is the band gap energy of the semiconductor calculated from the DR-UV−vis spectra. The conduction band edge potential (E_{CB}) was obtained using

$$E_{CB} = E_{VB} - E_g$$

By applying this method, the CB and VB potentials where calculated to be −0.23 and 2.17 eV for SnS_2 and −0.28 and 2.90 eV for TiO_2, respectively. (For band edge estimation, Supporting Information for details.) Although they may not be the absolute CB and VB potentials, the values extracted herein are in good agreement with the values reported in the literature for SnS_2 and anatase TiO_2.[37,40,70] Therefore, they can be used as guides offering a correct estimation of the relative band edge positions. A schematic diagram of SnS_2 and TiO_2 band edge energy-level configuration is illustrated in Figure S8 on the basis of the values derived from the above calculations.

On the basis of the data presented in Figure 8, electronic properties cannot fully interpret the photocatalytic efficiency, suggesting that light absorption is not here the dominant parameter determining photocatalytic activity. A closer view of the activity results suggests that TiO_2 has a crucial role in the photocatalytic degradation of DES by the SnS_2/TiO_2 nanostructures because pure TiO_2 and all SnS_2/TiO_2 samples exhibit higher activity than SnS_2. Furthermore, given that the CB of TiO_2 is slightly more negative whereas the VB is much more positive than that of SnS_2 the driving force of h^+ migration from TiO_2 to SnS_2 is expected to be much higher compared to that of e^- transfer via interface. Therefore, efficient charge separation may occur through the strong interfacial interaction in the SnS_2/TiO_2 heterostructures, reducing the photogenerated charge recombination rate and therefore improving the photocatalytic activity. The photogenerated charge transfer process in the SnS_2/TiO_2 heterostructures is also included in Figure S8. In a scheme like this, the e^- in TiO_2 can be captured by O_2 on the surface of the catalyst resulting in the formation reactive oxygen-based radicals, such as $O_2^{-\cdot}$. The $O_2^{-\cdot}$ upon protonation produces hydroperoxy radicals ($HO^{-2\cdot}$) and eventually hydroxyl radicals ($OH^{\cdot}$) are formed.[2] The increased number of h^+ in the SnS_2 VB can be used as oxidizing agents, producing $OH^{\cdot}$.[37] The remaining h^+ in the TiO_2 VB can either directly oxidize DES or react with adsorbed water molecules and surface OH-groups, producing $OH^{\cdot}$.[2]

On the basis of the above observation and on the schematic diagram of SnS_2 and TiO_2 band edge positions (Figure S8), the catalytic activity can be explained considering two parameters: (a) the exposed and accessible by DES TiO_2 surface and (b) the presence of SnS_2 for efficient separation of charge carriers. The actual content of the two components (SnS_2 and TiO_2) in the final SnS_2/TiO_2 hierarchical nanostructure would control the catalytic activity. Samples with no or high SnS_2 content are less active than those with moderate SnS_2 content, where efficient charge carrier separation can occur and relatively high TiO_2 surface is exposed to the substrate. High content of SnS_2 can lead to shielding of the active sites on the Ti nanofibers, preventing them from adsorbing DES and O_2 molecules, and the role of electron scavenger of such molecules was consequently reduced so that interfacial migration of photogenerated e^- to SnS_2 was favored. Therefore, considering the faster interfacial transfer of h^+ to SnS_2, this resulted in an increase in the e^-/h^+ pair recombination rate at or near the SnS_2/TiO_2 interface. Furthermore, because SnS_2 is a direct semiconductor with relatively narrow E_g, high SnS_2 loading might also facilitate the e^-/h^+ pair recombination within SnS_2, leading eventually to decreased photoactivity. This could also explain the low activity of the pure SnS_2 nanosheets (Figure 8).

CONCLUSIONS

1D SnS_2/TiO_2 hierarchical nanostructures made of anatase TiO_2 nanofibers decorated with nanometer-thick hexagonal SnS_2 nanosheets were synthesized by a facile one-step soft hydrothermal process, starting from H-titanate as preshaped Ti precursor. The SnS_2/TiO_2 nanofiber photocatalysts were proven highly efficient in the gas-phase photocatalytic degradation of DES under artificial solar light irradiation. The photocatalytic activity is proposed to be controlled by the actual content of SnS_2 nanosheets at the surface of the anatase TiO_2 nanofibers. A clear beneficial effect on photoactivity was observed for the hierarchical nanostructures with moderate SnS_2 content. The improved photocatalytic activity of the prepared nanostructures was triggered by the efficient separation of the photogenerated charge carriers, driven by the differences in the band edge positions (CB vs VB) and the tight interface within the coupled heterostructure as confirmed by XPS and HRTEM. SnS_2 did not operate as visible light sensitizer for TiO_2 but rather as oxidizing agent and charge carrier separator.

■ ASSOCIATED CONTENT

Ⓢ Supporting Information

The Supporting Information is available free of charge on the ACS Publications website at DOI: 10.1021/acsami.5b05370.

> Emission spectrum of the lamp. Ti 2p, O 1s, Sn 3d, and S 2p core-level binding energies. Photocatalysts characteristics: Sn/Ti nominal atomic ratio, Sn/Ti bulk atomic ratio (ICP-AES), Sn/Ti surface atomic ratio (XPS), BET surface area and band gap energy. Band gap analysis and DR-UV−vis spectra. Time on stream evolution of photocatalytic efficiency. Ti 2p, Sn 3d, O 1s, and S 2p XPS spectra of used photocatalysts. Correlation plot of O−S XPS peak vs activity. Band structure calculation details and band edge schematic representation. (PDF)

■ AUTHOR INFORMATION

Corresponding Author

*E-mail: nkeller@unistra.fr.

Funding

We acknowledge the support of the French Agence Nationale de la Recherche (ANR) under reference ANR-11-SECU-0003, and of the Direction Générale de l'Armement (DGA).

Notes

The authors declare no competing financial interest.

■ ACKNOWLEDGMENTS

We thank T. Romero (ICPEES) and S. Moldovan (IPCMS) for performing SEM and TEM analyses, respectively.

■ REFERENCES

(1) Smith, B. M. Catalytic Methods for the Destruction of Chemical Warfare Agents Under Ambient Conditions. *Chem. Soc. Rev.* **2008**, *37*, 470−478.

(2) Ollis, D.; Pichat, P.; Serpone, N. TiO_2 photocatalysis-25 years. *Appl. Catal., B* **2010**, *99*, 377.

(3) Li, J.; Singh, V. V.; Sattayasamitsathit, S.; Orozco, J.; Kaufmann, K.; Dong, R.; Gao, W.; Jurado-Sanchez, B.; Fedorak, Y.; Wang, J. Water-Driven Micromotors for Rapid Photocatalytic Degradation of Biological and Chemical Warfare Agents. *ACS Nano* **2014**, *8*, 11118−11125.

(4) Grandcolas, M.; Louvet, A.; Keller, N.; Keller, V. Layer-By-Layer Deposited Titanate-Based Nanotubes for Solar Photocatalytic Removal of Chemical Warfare Agents from Textiles. *Angew. Chem., Int. Ed.* **2009**, *48*, 161−164.

(5) Grandcolas, M.; Cottineau, T.; Louvet, A.; Keller, N.; Keller, V. Solar Light-Activated Photocatalytic Degradation of Gas Phase Diethylsulfide on WO_3-Modified TiO_2 Nanotubes. *Appl. Catal., B* **2013**, *138*−*139*, 128−140.

(6) Vorontsov, A. V.; Savinov, E. V.; Davydov, L.; Smirniotis, P. G. Photocatalytic Destruction of Gaseous Diethyl Sulfide Over TiO_2. *Appl. Catal., B* **2001**, *32*, 11−24.

(7) Vorontsov, A. V.; Lion, C.; Savinov, E. N.; Smirniotis, P. G. Pathways of Photocatalytic Gas Phase Destruction of HD Simulant 2-Chloroethyl Ethyl Sulfide. *J. Catal.* **2003**, *220*, 414−423.

(8) Kozlov, D.; Vorontsov, A. V.; Smirniotis, P. G.; Savinov, E. N. Gas-Phase Photocatalytic Oxidation of Diethyl Sulfide over TiO_2: Kinetic Investigations and Catalyst Deactivation. *Appl. Catal., B* **2003**, *42*, 77−96.

(9) Cojocaru, B.; Parvulescu, V. I.; Preda, E.; Iepure, G.; Somoghi, V.; Carbonell, E.; Alvaro, M.; Garcia, H. Sensitizers on Inorganic Carriers for Decomposition of the Chemical Warfare Agent Yperite. *Environ. Sci. Technol.* **2008**, *42*, 4908−4913.

(10) Neatu, S.; Parvulescu, V. I.; Epure, G.; Petrea, N.; Somoghi, V.; Ricchiardi, G.; Bordiga, S.; Zecchina, A. M/TiO_2/SiO_2 (M = Fe, Mn, And V) Catalysts in Photo-Decomposition of Sulfur Mustard. *Appl. Catal., B* **2009**, *91*, 546−554.

(11) Mera, N.; Hirakawa, T.; Sano, T.; Takeuchi, K.; Ichinose, H.; Seto, Y.; Negishi, N. Continuous Elimination Of Gaseous Dimethyl Methylphosphonate by a Photocatalytic Flow Reaction System. *Appl. Catal., B* **2014**, *146*, 71−78.

(12) Hirakawa, T.; Sato, K.; Komano, A.; Kishi, S.; Nishimoto, C. K.; Mera, N.; Kugishima, M.; Sano, T.; Ichinose, H.; Negishi, N.; Seto, Y.; Takeuchi, K. Experimental Study on Adsorption and Photocatalytic Decomposition of Isopropyl Methylphosphonofluoridate at Surface of TiO_2 Photocatalyst. *J. Phys. Chem. C* **2010**, *114*, 2305−2314.

(13) Kubacka, A.; Fernandez-Garcia, M.; Colon, G. Advanced Nanoarchitectures for Solar Photocatalytic Applications. *Chem. Rev.* **2012**, *112*, 1555−1614.

(14) Carp, O.; Huisman, C. L.; Reller, A. Photoinduced Reactivity of Titanium Dioxide. *Prog. Solid State Chem.* **2004**, *32*, 33−177.

(15) Shaham Waldmann, N.; Paz, Y. Photocatalytic Reduction of Cr(VI) by Titanium Dioxide Coupled to Functionalized CNTs: an Example of Counterproductive Charge Separation. *J. Phys. Chem. C* **2010**, *114*, 18946−18952.

(16) Yang, D.; Zhao, J.; Liu, H.; Zheng, Z.; Adebajo, M. O.; Wang, H.; Liu, X.; Zhang, H.; Zhao, J.-C.; Bell, J.; Zhu, H. Enhancing Photoactivity of TiO_2(B)/Anatase Core−Shell Nanofibers by Selectively Doping Cerium Ions into the TiO_2(B) Core. *Chem. - Eur. J.* **2013**, *19*, 5113−5119.

(17) Yang, D. J.; Liu, H. W.; Zheng, Z. F.; Yuan, Y.; Zhao, J. C.; Waclawik, E. R.; Ke, X. B.; Zhu, H. Y. An Efficient Photocatalyst Structure: TiO_2 (B) Nanofibers with a Shell of Anatase Nanocrystals. *J. Am. Chem. Soc.* **2009**, *131*, 17885−17893.

(18) Choi, W.; Termin, A.; Hoffmann, M. R. The Role of Metal Ion Dopants in Quantum-Sized TiO_2: Correlation Between Photoreactivity and Charge Carrier Recombination Dynamics. *J. Phys. Chem.* **1994**, *98*, 13669−13679.

(19) Zhang, J.; Xiao, F.-X.; Xiao, G.; Liu, B. Self-Assembly of a Ag Nanoparticle-Modified and Graphene-Wrapped TiO_2 Nanobelt Ternary Heterostructure: Surface Charge Tuning Toward Efficient Photocatalysis. *Nanoscale* **2014**, *6*, 11293−11302.

(20) Gu, H.; Yang, Y.; Tian, J.; Shi, G. Photochemical Synthesis of Noble Metal (Ag, Pd, Au, Pt) On Graphene/ZnO Multihybrid Nanoarchitectures as Electrocatalysis for H_2O_2 Reduction. *ACS Appl. Mater. Interfaces* **2013**, *5*, 6762−6768.

(21) Christoforidis, K. C.; Figueroa, S. J. A.; Fernandez-Garcia, M. Iron−Sulfur Codoped TiO_2 Anatase Nano-Materials: UV and Sunlight Activity for Toluene Degradation. *Appl. Catal., B* **2012**, *117-118*, 310.

(22) Serpone, N.; Borgarello, E.; Grätzel, M. Visible Light Induced Generation of Hydrogen from H_2S in Mixed Semiconductor Dispersions; Improved Efficiency Through Inter-Particle Electron Transfer. *J. Chem. Soc., Chem. Commun.* **1984**, 342−344.

(23) Di Paola, A.; Bellardita, M.; Ceccato, R.; Palmisano, L.; Parrino, F. Highly Active Photocatalytic TiO_2 Powders Obtained by Thermohydrolysis of $TiCl_4$ In Water. *J. Phys. Chem. C* **2009**, *113*, 15166−15174.

(24) Ikeda, S.; Sugiyama, N.; Pal, B.; Marci, G.; Palmisano, L.; Noguchi, H.; Uosaki, K.; Ohtani, B. Photocatalytic Activity of Transition-Metal-Loaded Titanium(IV) Oxide Powders Suspended in Aqueous Solutions: Correlation with Electron−Hole Recombination Kinetics. *Phys. Chem. Chem. Phys.* **2001**, *3*, 267−273.

(25) Berger, T.; Diwald, O.; Knözinger, E.; Sterrer, M.; Yates, J. T., Jr. UV Induced Local Heating Effects in TiO_2 Nanocrystals. *Phys. Chem. Chem. Phys.* **2006**, *8*, 1822−1826.

(26) Ke, S.-C.; Wang, T.-C.; Wong, M.-S.; Gopal, N. O. Low Temperature Kinetics and Energetics of the Electron and Hole Traps in Irradiated TiO_2 Nanoparticles as Revealed by EPR Spectroscopy. *J. Phys. Chem. B* **2006**, *110*, 11628−11634.

(27) Hurum, D. C.; Gray, K. A.; Rajh, T.; Thurnauer, M. C. Recombination Pathways in the Degussa P25 Formulation of TiO_2: Surface Versus Lattice Mechanisms. *J. Phys. Chem. B* **2005**, *109*, 977−980.

(28) Scotti, R.; Bellobono, I. R.; Canevali, C.; Cannas, C.; Catti, M.; D'Arienzo, M.; Musinu, A.; Polizzi, S.; Sommariva, M.; Testino, A.; Morazzoni, F. Sol−Gel Pure and Mixed-Phase Titanium Dioxide for Photocatalytic Purposes: Relations Between Phase Composition, Catalytic Activity, and Charge-Trapped Sites. *Chem. Mater.* **2008**, *20*, 4051−4061.

(29) Wu, K.; Zhu, H.; Liu, Z.; Rodriguez-Cordoba, W.; Lian, T. Ultrafast Charge Separation and Long-Lived Charge Separated State in Photocatalytic CdS−Pt Nanorod Heterostructures. *J. Am. Chem. Soc.* **2012**, *134*, 10337−10340.

(30) Zhang, J.; Yu, J.; Zhang, Y.; Li, Q.; Gong, J. R. Visible Light Photocatalytic H_2-Production Activity of CuS/ZnS Porous Nanosheets Based on Photoinduced Interfacial Charge Transfer. *Nano Lett.* **2011**, *11*, 4774−4779.

(31) Yu, J.; Xu, C.-Y.; Ma, F.-X.; Hu, S.-P.; Zhang, Y.-W.; Zhen, L. Monodisperse SnS_2 Nanosheets for High-Performance Photocatalytic Hydrogen Generation. *ACS Appl. Mater. Interfaces* **2014**, *6*, 22370−22377.

(32) Sun, Y.; Cheng, H.; Gao, S.; Sun, Z.; Liu, Q.; Liu, Q.; Lei, F.; Yao, T.; He, J.; Wei, S.; Xie, Y. Freestanding Tin Disulfide Single-Layers Realizing Efficient Visible-Light Water Splitting. *Angew. Chem., Int. Ed.* **2012**, *51*, 8727−8731.

(33) Tsuji, I.; Kato, H.; Kudo, A. Visible-Light-Induced H_2 Evolution From An Aqueous Solution Containing Sulfide and Sulfite over a ZnS−$CuInS_2$−Ag InS_2 Solid-Solution. *Angew. Chem., Int. Ed.* **2005**, *44*, 3565−3568.

(34) Wang, X.; Liu, G.; Chen, Z.-G.; Li, F.; Wang, L.; Lu, G. Q.; Cheng, H.-M. Enhanced Photocatalytic Hydrogen Evolution by Prolonging the Lifetime of Carriers in ZnO/CdS Heterostructures. *Chem. Commun.* **2009**, 3452−3454.

(35) Yang, F.; Han, G.; Fu, D.; Chang, Y.; Wang, H. Improved Photodegradation Activity of TiO_2 via Decoration With SnS_2 Nanoparticles. *Mater. Chem. Phys.* **2013**, *140*, 398−404.

(36) Sun, M.; Yan, Q.; Yan, T.; Li, M.; Wei, D.; Wang, Z.; Wei, Q.; Du, B. Facile Fabrication of 3D Flower-Like Heterostructured g-C_3N_4/SnS_2 Composite with Efficient Photocatalytic Activity Under Visible Light. *RSC Adv.* **2014**, *4*, 31019−31027.

(37) Zhang, Z.; Shao, C.; Li, X.; Sun, Y.; Zhang, M.; Mu, J.; Zhang, P.; Guo, Z.; Liu, Y. Hierarchical Assembly of Ultrathin Hexagonal SnS_2 Nanosheets onto Electrospun TiO_2 Nanofibers: Enhanced Photocatalytic Activity Based on Photoinduced Interfacial Charge Transfer. *Nanoscale* **2013**, *5*, 606−618.

(38) Liu, H.; Su, Y.; Chen, P.; Wang, Y. Microwave-Assisted Solvothermal Synthesis of 3D Carnation-Like SnS_2 Nanostructures with High Visible Light Photocatalytic. *J. Mol. Catal. A: Chem.* **2013**, *378*, 285−292.

(39) Zhang, Y. C.; Yao, L.; Zhang, G.; Dionysiou, D. D.; Li, J.; Du, X. One-Step Hydrothermal Synthesis of High-Performance Visible-Light-Driven SnS_2/SnO_2 Nanoheterojunction Photocatalyst for the Reduction of Aqueous Cr(VI). *Appl. Catal., B* **2014**, *144*, 730−738.

(40) Zhang, Y. C.; Du, Z. N.; Li, K. W.; Zhang, M.; Dionysiou, D. D. High-Performance Visible-Light-Driven SnS_2/SnO_2 Nanocomposite Photocatalyst Prepared via in Situ Hydrothermal Oxidation of SnS_2 Nanoparticles. *ACS Appl. Mater. Interfaces* **2011**, *3*, 1528−1537.

(41) Wang, J.; Li, X.; Li, X.; Zhu, J.; Li, H. Mesoporous Yolk−Shell SnS_2−TiO_2 Visible Photocatalysts with Enhanced Activity and Durability in Cr(VI) Reduction. *Nanoscale* **2013**, *5*, 1876−1881.

(42) Chen, P.; Su, Y.; Liu, H.; Wang, Y. Interconnected Tin Disulfide Nanosheets Grown on Graphene for Li-Ion Storage and Photocatalytic Applications. *ACS Appl. Mater. Interfaces* **2013**, *5*, 12073−12082.

(43) Kang, J.-G.; Lee, G.-H.; Park, K.-S.; Kim, S.-O.; Lee, S.; Kim, D.-W.; Park, J.-G. Three-Dimensional Hierarchical Self-Supported Multi-Walled Carbon Nanotubes/Tin(IV) Disulfide Nanosheets Heterostructure Electrodes for High Power Li Ion Batteries. *J. Mater. Chem.* **2012**, *22*, 9330−9337.

(44) Yella, A.; Mugnaioli, E.; Panthofer, M.; Therese, H. A.; Kolb, U.; Tremel, W. Bismuth-Catalyzed Growth of SnS_2 Nanotubes and Their Stability. *Angew. Chem., Int. Ed.* **2009**, *48*, 6426−6430.

(45) Zhai, C.; Du, N.; Yang, H. Z. Large-Scale Synthesis of Ultrathin Hexagonal Tin Disulfide Nanosheets with Highly Reversible Lithium Storage. *Chem. Commun.* **2011**, *47*, 1270−1272.

(46) Cantau, C.; Larribau, S.; Pigot, T.; Simon, M.; Maurette, M. T.; Lacombe, S. Oxidation of Nauseous Sulfur Compounds by Photocatalysis or Photosensitization. *Catal. Today* **2007**, *122*, 27−38.

(47) Scofield, J. H. Hartree-Slater Subshell Photoionization Cross-Sections at 1254 and 1487 eV. *J. Electron Spectrosc. Relat. Phenom.* **1976**, *8*, 129−137.

(48) Keller, V.; Bernhardt, P.; Garin, F. Photocatalytic Oxidation of Butyl Acetate in Vapor Phase on TiO_2, Pt/TiO_2 and WO_3/TiO_2 Catalysts. *J. Catal.* **2003**, *215*, 129−138.

(49) Wang, H.; Shao, W.; Gu, F.; Zhang, L.; Lu, M.; Li, C. Synthesis of Anatase TiO_2 Nanoshuttles by Self-Sacrificing of Titanate Nanowires. *Inorg. Chem.* **2009**, *48*, 9732−9736.

(50) Kolen'ko, Y. V.; Kovnir, K. A.; Gavrilov, A. I.; Garshev, A. V.; Frantti, J.; Lebedev, O. I.; Churagulov, B. R.; Van Tendeloo, G.; Yoshimura, M. Hydrothermal Synthesis and Characterization of Nanorods of Various Titanates and Titanium Dioxide. *J. Phys. Chem. B* **2006**, *110*, 4030−4038.

(51) Christoforidis, K. C.; Iglesias-Juez, A.; Figueroa, S. J. A.; Di Michiel, M.; Newton, M. A.; Fernandez-Garcia, M. Structure and Activity of Iron-Doped TiO_2-Anatase Nanomaterials for Gas-Phase Toluene Photo-Oxidation. *Catal. Sci. Technol.* **2013**, *3*, 626−634.

(52) Lucovsky, G.; Mikkelsen, J. C., Jr.; et al. Optical Phonon Anisotropies in the Layer Crystals SnS_2 and $SnSe_2$. *Phys. Rev. B Solid State* **1976**, *14*, 1663−1669.

(53) Price, L. S.; Parkin, I. P.; Hardy, A. M. E.; Clark, R. J. H.; et al. Atmospheric Pressure Chemical Vapor Deposition of Tin Sulfides (SnS, Sn_2S_3, and SnS_2) on Glass. *Chem. Mater.* **1999**, *11*, 1792−1799.

(54) Zhang, Y.; Xu, J.; Feng, J.; Yang, A.; Liu, Y.; Zhi, M.; Hong, Z. Enhanced Photocatalytic Degradation of Methyl Orange in TiO_2(B)@Anatase Heterostructure Nanocomposites Prepared by a Facile Hydrothermal Method. *Mater. Lett.* **2013**, *112*, 173−176.

(55) Zhu, H. Y.; Lan, Y.; Gao, X. P.; Ringer, S. P.; Zheng, Z. F.; Song, D. Y.; Zhao, J. C. Phase Transition Between Nanostructures of Titanate and Titanium Dioxides via Simple Wet-Chemical Reactions. *J. Am. Chem. Soc.* **2005**, *127*, 6730−6736.

(56) Wen, B.-M.; Liu, C.-Y.; Liu, Y. Solvothermal Synthesis of Ultralong Single-Crystalline TiO_2 Nanowires. *New J. Chem.* **2005**, *29*, 969−671.

(57) Mao, Y.; Wong, S. S. Size- and Shape-Dependent Transformation of Nanosized Titanate Into Analogous Anatase Titania Nanostructures. *J. Am. Chem. Soc.* **2006**, *128*, 8217−8226.

(58) Zhu, H. Y.; Gao, X. P.; Lan, Y.; Song, D. Y.; Xi, Y. X.; Zhao, J. C. Hydrogen Titanate Nanofibers Covered with Anatase Nanocrystals: A Delicate Structure Achieved by the Wet Chemistry Reaction of the Titanate Nanofibers. *J. Am. Chem. Soc.* **2004**, *126*, 8380−8381.

(59) Wen, P. H.; Itoh, H.; Tang, W. P.; Feng, Q. Single Nanocrystals of Anatase-Type TiO_2 Prepared from Layered Titanate Nanosheets: Formation Mechanism and Characterization of Surface Properties. *Langmuir* **2007**, *23*, 11782−11790.

(60) Colon, G.; Hidalgo, M. C.; Munuera, G.; Ferino, I.; Cutrufello, M. G.; Navio, J. A. Structural and Surface Approach to the Enhanced Photocatalytic Activity of Sulfated TiO_2 Photocatalyst. *Appl. Catal., B* **2006**, *63*, 45−59.

(61) Zhang, Y. C.; Li, J.; Xu, H. Y. One-Step in Situ Solvothermal Synthesis of SnS_2/TiO_2 Nanocomposites with High Performance in Visible Light-Driven Photocatalytic Reduction of Aqueous Cr(VI). *Appl. Catal., B* **2012**, *123*−*124*, 18−26.

(62) Qin, G.; Zhang, X.; Wang, C. Design of Nitrogen Doped Graphene Grafted TiO_2 Hollow Nanostructures with Enhanced Sodium Storage Performance. *J. Mater. Chem. A* **2014**, *2*, 12449−12458.

(63) Pian, X.; Lin, B.; Chen, Y.; Kuang, J.; Zhang, K.; Fu, L. Pillared Nanocomposite TiO_2/Bi-Doped Hexaniobate with Visible-Light Photocatalytic Activity. *J. Phys. Chem. C* **2011**, *115*, 6531−6539.

(64) Spadavecchia, F.; Cappelletti, G.; Ardizzone, S.; Bianchi, C. L.; Cappelli, S.; Oliva, C.; et al. Solar Photoactivity of Nano-N-TiO_2 from Tertiary Amine: Role of Defects and Paramagnetic Species. *Appl. Catal., B* **2010**, *96*, 314−322.

(65) Dong, W.; Lee, C. W.; Lu, X.; Sun, Y.; Hua, W.; Zhuang, G.; Zhang, S.; Chen, J.; Hou, H.; Zhao, D. Synchronous Role of Coupled Adsorption and Photocatalytic Oxidation on Ordered Mesoporous Anatase TiO_2−SiO_2 Nanocomposites Generating Excellent Degradation Activity of RhB Dye. *Appl. Catal., B* **2010**, *95*, 197−207.

(66) Wodka, D.; Bielanska, E.; Socha, R. P.; Elżbieciak-Wodka, M. E.; Gurgul, J.; Nowak, P.; et al. Photocatalytic Activity of Titanium Dioxide Modified by Silver Nanoparticles. *ACS Appl. Mater. Interfaces* **2010**, *2*, 1945−1953.

(67) Alonso-Tellez, A.; Robert, D.; Keller, N.; Keller, V. A Parametric Study of the UV-A Photocatalytic Oxidation of H_2S over TiO_2. *Appl. Catal., B* **2012**, *115*−*116*, 209−218.

(68) González-García, N.; Ayllon, J. A.; Domenech, X.; Peral, J. TiO_2 Deactivation During the Gas-Phase Photocatalytic Oxidation of Dimethyl Sulfide. *Appl. Catal., B* **2004**, *52*, 69−77.

(69) Lin, X.; Xing, J.; Wang, W.; Shan, Z.; Xu, F.; Huang, F. Photocatalytic Activities of Heterojunction Semiconductors $Bi_2O_3/BaTiO_3$: A Strategy for the Design of Efficient Combined Photocatalysts. *J. Phys. Chem. C* **2007**, *111*, 18288−18293.

(70) Gratzel, M. Photoelectrochemical Cells. *Nature* **2001**, *414*, 338−344.